

SDSS OBSERVATIONS OF KUIPER BELT OBJECTS: COLORS AND VARIABILITY

ERAN O. OFEK^{1,2,3}

Accepted to ApJ

ABSTRACT

Colors of Trans Neptunian Objects (TNOs) are used to study the evolutionary processes of bodies in the outskirts of the Solar System, and to test theories regarding their origin. Here I describe a search for serendipitous Sloan Digital Sky Survey (SDSS) observations of known TNOs and Centaurs. I present a catalog of SDSS photometry, colors and astrometry of 388 measurements of 42 outer Solar-System objects. I find a weak evidence, at the $\approx 2\sigma$ level (per trial), for a correlation between the $g-r$ color and inclination of scattered disk objects and hot classical KBOs. I find a correlation between the $g-r$ color and the angular momentum in the z direction of all the objects in this sample. These findings should be verified using larger samples of TNOs. Light curves as a function of phase angle are constructed for 13 objects. The steepness of the slopes of these light curves suggests that the coherent backscatter mechanism plays a major role in the reflectivity of outer Solar-System small objects at small phase angles. I find a weak evidence for an anti-correlation, significant at the 2σ confidence level (per trial), between the g -band phase angle slope parameter and the semi-major axis, as well as the aphelion distance, of these objects (i.e., they show a more prominent “opposition effect” at smaller distances from the Sun). However, this plausible correlation should be verified using larger sample. I discuss the origin of this possible correlation and argue that if this correlation is real it probably indicates that “Sedna”-like objects have a different origin than other classes of TNOs. Finally, I identify several objects with large variability amplitudes.

Subject headings: solar system: general — solar system: Kuiper Belt — techniques: photometric

1. INTRODUCTION

Colors and variability of small bodies in the outer Solar System provide insight into the physical properties and evolution of these objects. The colors of these objects are believed to be related to evolutionary processes such as collisions, resurfacing and the interaction of cosmic rays with the surface of these bodies (e.g., Cooper et al. 2003; see however Porter et al. 2010). The large body of color observations of Trans Neptunian Object (TNOs; e.g., Luu & Jewitt 1996; Delsanti et al. 2001; Hainaut & Delsanti 2002; Trujillo & Brown 2002; Tegler & Romanishin 2003; Almeida et al. 2009; Santos-Sanz et al. 2009; Romanishin et al. 2010; Sheppard 2010) is not entirely consistent with theoretical ideas (see the review in Jewitt, Morbidelli & Rauer 2008). The main characteristic of TNO colors is diversity. To date, the only secure correlation involving TNO colors is between the $B-I_c$ color and the orbital inclination of classical Kuiper Belt Objects (KBOs) and scattered disk objects⁴ (e.g., Hainaut & Delsanti 2002; Trujillo & Brown 2002; Peixinho et al. 2008). I note that the reported correlations between the inclination and $V-R_c$ or R_c-I_c colors remain controversial (e.g., Stephens et al. 2003).

KBO variability is related to shape, binarity and albedo surface uniformity. Measuring the binary frequency allows of testing models of KBO binary formation (e.g. Goldreich, Lithwick & Sari 2002; Weidenschilling 2002). Moreover, in some cases binaries are used to determine masses (e.g., Noll

et al. 2004) and densities (e.g., Sheppard & Jewitt 2004; Gnat & Sari 2010) of KBOs.

TNO variability studies typically require medium size telescopes and are therefore observationally demanding. The Sloan Digital Sky Survey (SDSS; York et al. 2000) provides imaging in the $ugriz$ -bands of a considerable fraction of the celestial sphere. The photometric calibration of the SDSS is good to $\approx 1\%$ in the $griz$ bands and $\approx 2\%$ in the u band (e.g., Tucker et al. 2006; Padmanabhan et al. 2008). The SDSS astrometric accuracy is $\approx 0.1''$ (e.g., Pier et al. 2003). However, given the short time interval within which the SDSS images were obtained (≈ 5 min), it does not allow in most cases the detection of KBO motion⁵. Ivezić et al. (2001) and Juric et al. (2001) constructed a catalog of all the SDSS sources displaying a significant motion within the 5 min exposures—the SDSS Moving Object Catalog⁶ (SDSSMOC). However, in the fourth release of this catalog (SDSSMOC4) there are only 33 entries of known objects with $a > 10$ AU.

Here I describe a search for known small objects in the outer parts of the Solar System in the existing SDSS imaging data. A compilation of the photometric and astrometric properties of these bodies are presented and analyzed. The structure of this paper is as follows. In §2 I describe the catalog of SDSS observations of outer Solar-System objects. In §3 I discuss their colors, while in §4 I describe their variability properties. Finally, I summarize the results in §5.

2. A CATALOG OF SDSS OBSERVATIONS OF TNOs

This section describes the construction of a catalog of SDSS observations of known outer Solar-System objects with semi-major axes $a > 10$ AU.

⁵ At opposition, the typical geocentric on sky motion of a Solar-System object orbiting the Sun at 40 AU is $\sim 0.25''$ in 5 min

⁶ <http://www.astro.washington.edu/users/ivezic/sdssmoc/sdssmoc.html>

¹ Division of Physics, Mathematics and Astronomy, California Institute of Technology, Pasadena, CA 91125, USA

² Einstein Fellow

³ Benoziyo Center for astrophysics, Weizmann Institute of Science, 76100 Rehovot, Israel.

⁴ Here TNOs are defined as objects with semi-major axis larger than that of Neptune. KBOs and scattered disk objects are loosely defined and here we follow the definition of Morbidelli & Brown (2004).

2.1. SDSS images whose footprints may contain known TNOs

I retrieved a list of the orbital elements of all known (numbered and unnumbered) minor planets in the Solar System⁷ from the Jet Propulsion Laboratory (JPL) Horizons⁸ system (updated for 2010 August 2). Then, I selected all the objects with semi-major axis $a > 10$ AU. This list contains 1469 bodies.

I used the SDSS (York et al. 2000) CasJobs⁹ utility to generate a catalog of all the images¹⁰ which are available in the SDSS database. Here, an “image” is defined uniquely by the SDSS run, rerun, camcol (camera column), and field¹¹. The catalog contains all the images included in the SDSS data release 7 (DR7), Segue, and Stripe 82 (Abazajian et al. 2009). For each image I obtained the time at which it was observed and I calculated the coordinates of its four corners¹².

Next, I used the JPL Horizons system to generate daily ephemerides for each of the 1469 objects between Julian Day (JD) 2451070 and 2454467. This JD range contains all the SDSS observations in DR7. For each entry in the daily ephemerides of each object I checked whether it is contained within any of the polygons defining the corners of all the SDSS images taken within one day of the ephemeris entry. If a match was found, then the object ephemeris was regenerated for the exact time at which the image was taken (to an accuracy of 1 min). In total, 4642 possible observations of 574 outer Solar-System objects were found. Of these 845 entries are of objects with a predicted V -band magnitude, at the time of observation, brighter than $V_{\text{pred}} = 22$ mag.

2.2. Photometry and astrometry of TNOs in SDSS images

Next, I searched for sources in the SDSS images near the predicted position of the outer Solar-System objects. Unlike “typical” minor planet surveys, this method only yields a single image per object per field, so one cannot use the motion of the object between two images of the same field to verify whether it is indeed a Solar-System object (rather than a variable star or a transient). Therefore, as described below, I exercised great care to remove false identifications or contamination by nearby sources.

For each entry in the catalog of SDSS images possibly containing an observation of a Solar-System object with a predicted magnitude brighter than $V_{\text{pred}} = 22.0$ (§2.1), I downloaded the SDSS source catalog corresponding to that image¹³. Then I searched for all the SDSS sources within $8''$ of the predicted position of the object. Figure 1 shows the distribution of the angular separations between the predicted object position and the nearest SDSS source.

In order to remove photometric measurements contaminated by nearby sources and possible false detections, I selected only sources which have exactly one SDSS match within $8''$ of the outer Solar-System object predicted position. I further demanded that this SDSS source is within $1.5''$ from the predicted position of the object. Moreover, I selected only

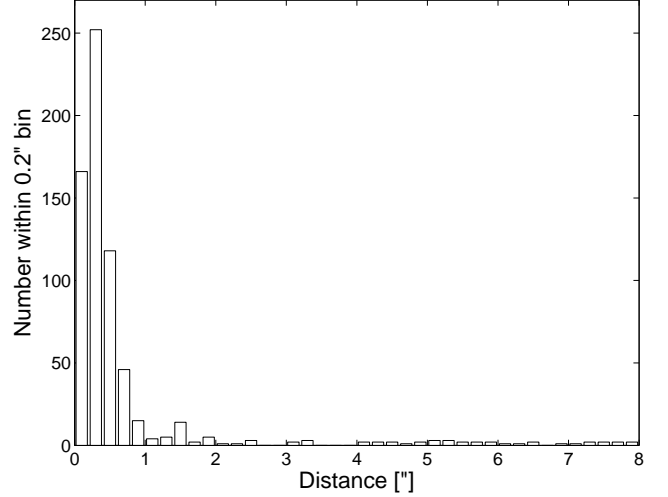


FIG. 1.— Histogram of angular distances between the predicted position of the Solar-System objects and the position of the SDSS source nearest to the predicted position (either the Solar-System object or a background object). This plot is shown for 672 measurements in which I find at least one SDSS source within $8''$ of the predicted position of the object.

sources for which there are no USNO-B1 (Monet et al. 2003) objects within $8''$ from the position of the SDSS matched source. Finally, I removed from the list of SDSS matches entries with r -band magnitude errors larger than 0.2 mag. The final list contains 388 probable identifications of 42 unique outer Solar-System objects in SDSS images. Each of these objects has between 1 and 49 measurements. Table 1 presents the astrometric properties of the 388 identifications, while Table 2 lists all the predicted and measured photometry.

I also calculated the absolute planetary magnitude¹⁴, neglecting phase effects (see §4), $H_f = m_f - 5 \log_{10}(R\Delta)$, where m_f is the apparent magnitude in band f (u , g , r , i or z), R is the object’s heliocentric distance¹⁵, and Δ is its geocentric distance. The values of R , Δ and the phase angle β (defined as the Sun–target–observer angle), for each observation, are listed in Table 2. I also calculated the median, standard deviation (StD), and range of the absolute magnitude measurements (Table 2).

2.3. Verification

As shown in Figure 1, a large fraction of the matched SDSS sources are found within $1.5''$ from the predicted position of the Solar-System objects. In contrast, the probability for a match with background sources should increase as the square of the distance. Since the number of matches above $1.5''$ is small I argue that the fraction of false identification and contaminated photometry in Tables 1–2 is negligible. Furthermore, I note that assuming a source density of 10^4 deg^{-2} in the SDSS images, the probability of finding a source within $1.5''$ from a random position is 0.5%.

Nevertheless, as an additional test I uploaded cutouts of the SDSS images containing some of the candidates, along with SDSS images of the same sky positions taken at different epochs. If such an extra epoch image was not available then I uploaded instead an image from the Palomar Sky Sur-

⁷ http://ssd.jpl.nasa.gov/?sb_lem

⁸ <http://ssd.jpl.nasa.gov/?horizons>

⁹ <http://casjobs.sdss.org/casjobs/>

¹⁰ 1,589,702 images.

¹¹ see definitions in: <http://www.sdss.org/dr7/glossary/index.html>

¹² Performed by transforming the SDSS great circle coordinates to equatorial coordinates; <http://www.sdss.org/dr7/products/general/astrometry.html>

¹³ These are the tsObj files stored in <http://das.sdss.org/imaging/> which are described in <http://www.sdss.org/dr7.1/dm/flatFiles/tsObj.html>

¹⁴ Defined as the magnitude of an object observed at opposition and at 1 AU from the Sun and Earth.

¹⁵ Denoted by R to distinguish it from the SDSS r -band magnitude.

TABLE 1
ASTROMETRIC MEASUREMENTS OF SOLAR-SYSTEM OBJECTS IDENTIFIED IN SDSS IMAGES

Name	JD-2450000 day	Run	Rerun	Camcol	Field	α_{2000}^{obs} deg	δ_{2000}^{obs} deg	α_{2000}^{pred} deg	δ_{2000}^{pred} deg	Dist arcsec
24835	1464.856934	1035	40	4	126	24.909451	14.267754	24.909542	14.267833	0.43
26375	2318.829706	2986	40	3	273	159.458594	6.417053	159.458667	6.417111	0.34
	2338.709340	3015	40	3	300	159.008464	6.578481	159.008458	6.578528	0.17
35671	1819.838123	1755	40	2	340	354.611093	-0.825181	354.611083	-0.825139	0.16
	2196.787392	2649	40	2	94	355.871559	-0.418224	355.871583	-0.418222	0.09

NOTE. — Astrometric measurements of 388 identifications of 42 outer Solar-System objects. Name is the minor planet number or provisional designation, Run/Rerun/Camcol/Field identifies the unique SDSS *ugriz* image, while JD provides the time at which the *r*-band image was obtained. α and δ are the J2000.0 coordinates of the object, while superscript “obs” is for observed coordinates, and superscript “pred” is for predicted coordinates. Dist is the angular distance between the observed and predicted coordinates. This table is published in its entirety in the electronic edition of the *Astrophysical Journal*. A portion of the full table is shown here for guidance regarding its form and content.

TABLE 2
PHOTOMETRIC PROPERTIES OF SOLAR-SYSTEM OBJECTS IDENTIFIED IN SDSS IMAGES

Name	JD-2450000 day	<i>R</i> AU	Δ AU	β deg	V_{pred} mag	Type	<i>u</i> mag	<i>g</i> mag	<i>r</i> mag	<i>i</i> mag	<i>z</i> mag	Δu mag	Δg mag	Δr mag	Δi mag	Δz mag
24835	1464.856934	39.497	38.512	0.24	20.8	6	...	20.879	20.363	20.192	19.930	0.271	0.038	0.034	0.043	0.145
26375	2318.829706	34.179	33.221	0.42	20.1	6	...	20.859	20.087	19.755	19.634	0.269	0.033	0.025	0.026	0.059
	2338.709340	34.191	33.206	0.18	20.0	6	...	20.929	20.161	19.784	19.592	0.605	0.034	0.027	0.026	0.064
35671	1819.838123	38.156	37.188	0.38	21.6	6	...	21.760	21.262	21.140	...	0.425	0.076	0.062	0.074	0.275
	2196.787392	38.109	37.203	0.63	21.7	6	...	21.653	21.270	21.291	...	1.087	0.063	0.057	0.079	0.242

NOTE. — As in Table 1 except for the photometric properties. V_{pred} is the minor planet predicted *V*-band magnitude at the time of the SDSS observation. Type is the SDSS morphological classification (6: star; 3: galaxy). *ugriz* are the SDSS magnitudes, while their corresponding errors are Δu , Δg , Δr , Δi and Δz . In cases in which the error magnitudes are larger than 0.2 mag, I replaced the SDSS magnitude with the “no-data” symbol. However, I kept the errors in the table. Note that the absolute planetary *r*-band magnitude of measurement number 18 of object 145452, measurement number 7 of object 145453, and measurement number 13 of object 145480 deviate by more than one magnitude from the median absolute planetary magnitude and are probably bad measurements. These measurements are listed in this table but are not used in the subsequent analysis (e.g., they are not shown in Figure 3 and they are excluded from the phase-angle slope parameter fits summarized in Table 4). This table is published in its entirety in the electronic edition of the *Astrophysical Journal*. A portion of the full table is shown here for guidance regarding its form and content.

vey¹⁶ (Reid et al. 1991). I inspected by eye about 100 of these cutouts and verified that the Solar-System object candidate is indeed detected only in one epoch. Finally, I note that the differences between the predicted and measured magnitudes (Table 2) is typically small, on the order of 0.3 mag.

In Table 2 I list also the SDSS morphological type (6: star; 3: galaxy) for the TNOs. Some of the sources are identified as possible resolved objects. This is presumably because the reliability of SDSS star–galaxy separation degrades near the survey detection limit.

3. OBJECT COLOR

The absolute planetary magnitude of objects identified in SDSS images are listed in Table 3. If multiple-epoch observations are available, I adopt the median of the object magnitudes over all epochs as the object’s magnitude. In cases in which an object was observed in multiple epochs, I also give the standard deviation (StD) of the absolute magnitudes, and the range of the *r*-band absolute magnitudes. I note that the variability indicators in this table do not separate between variability due to phase-angle variations and other causes (e.g., rotation). Separation of phase-angle and rotation-induced variability is possible only when a large number of observations is available. Nevertheless, the variability indicators in this table give a rough idea regarding which objects may be variable and which objects are less likely to be variable. For objects which have more than ten observations more reliable variability indicators, which are cal-

culated after subtracting the phase-angle variations, are available in Table 5. Figure 2 shows the *g* – *r* vs. *r* – *i* color–color diagram for the 37 objects for which both *g* – *r* and *r* – *i* color measurements are available. The symbols indicate different subclasses of objects (see figure legend and caption). I note that the *g* – *r* vs. *r* – *i* locus of objects in Figure 2 is generally similar, but offset, relative to the *B* – *V* vs. *R* – *I* colors locus of TNOs (for comparison see Fig. 2 in Tegler & Romanishin 2003).

In order to explore possible correlations of the colors with orbital properties I calculated the Spearman rank correlation coefficients between the *g* – *r*, *r* – *i*, and *g* – *i* colors and various photometric and orbital properties of these objects and their subgroups (e.g., the groups listed in Fig. 2). This approach has the disadvantage that it introduce many trials, and reduces the significance of any reported correlation by a complicated way that depends on the correlations between the various parameters. Nevertheless, this may give us some ideas about where to look for correlations when larger samples, based on the same filters, become available. For each correlation I also calculated the probability of getting a value larger than the correlation coefficient. This was calculated from the correlation coefficients’ probability distributions derived from 10⁴ bootstrap simulations (Efron 1982; Efron & Tibshirani 1993). In each simulation, considering two lists “X” and “Y”, I select for each entry in X a random entry in Y and calculate the correlation between the two randomly permuted lists. I calculated the correlations of the three colors *g* – *r*, *r* – *i*, and *g* – *i* with the *r* – *i* color, H_r , semi-major axis *a*, orbital eccentricity *e*, orbital inclination *I*, perihelion distance *q*, aphelion

¹⁶ http://archive.stsci.edu/cgi-bin/dss_form

TABLE 3
MEAN PHOTOMETRIC PROPERTIES OF OUTER SOLAR-SYSTEM OBJECTS IDENTIFIED IN SDSS IMAGES

Name	N_{obs}^r	H_u mag	H_g mag	H_r mag	H_i mag	H_z mag	u_{StD} mag	g_{StD} mag	r_{StD} mag	i_{StD} mag	z_{StD} mag	r_{range} mag	a AU	e	I deg
24835	1	...	4.968	4.452	4.281	4.019	...	0.000	0.000	0.000	0.000	0.000	41.957	0.106	27.000
26375	2	...	5.619	4.848	4.494	4.337	...	0.050	0.052	0.021	0.029	0.073	55.108	0.415	7.631
35671	16	...	6.079	5.573	5.450	4.975	...	0.104	0.106	0.099	0.028	0.398	38.110	0.043	4.596
38628 (Huya)	1	...	5.600	4.775	4.394	4.249	...	0.000	0.000	0.000	0.000	0.000	39.373	0.276	15.488
65489 (Ceto)	1	...	7.182	6.519	6.136	5.893	...	0.000	0.000	0.000	0.000	0.000	99.676	0.821	22.325
73480	11	...	9.270	8.641	8.337	8.151	...	0.105	0.074	0.079	0.114	0.238	31.245	0.572	16.627
79360	4	...	6.187	5.287	4.773	0.132	0.155	0.054	...	0.325	43.739	0.008	2.250
82075	3	...	5.222	4.496	4.215	4.084	...	0.153	0.119	0.060	0.199	0.225	57.686	0.288	19.840
82155	1	...	6.634	6.141	5.693	0.000	0.000	0.000	...	0.000	84.625	0.617	12.739
82158	1	...	6.963	6.129	5.708	0.000	0.000	0.000	...	0.000	212.866	0.839	30.842
90482 (Orcus)	2	4.110	2.702	2.222	2.082	2.054	0.021	0.050	0.070	0.018	0.075	0.098	39.173	0.227	20.573
119878	2	...	7.120	6.216	5.674	5.198	...	0.135	0.040	0.046	0.000	0.056	53.648	0.344	15.759
120132	1	...	5.436	4.653	4.265	4.331	...	0.000	0.000	0.000	0.000	0.000	49.197	0.247	11.798
120181	2	...	8.118	7.309	6.845	0.043	0.075	0.043	...	0.106	32.536	0.177	2.717
135182	1	6.965	0.000	0.000	37.285	0.021	1.837
139775	10	...	7.806	7.047	6.593	0.067	0.197	0.225	...	0.644	39.649	0.199	6.480
144897	17	...	5.148	4.315	4.026	3.830	...	0.086	0.069	0.232	0.172	0.223	39.203	0.043	9.524
145451	27	5.996	4.852	4.436	4.289	4.283	0.251	0.084	0.070	0.084	0.126	0.321	91.720	0.617	28.759
145452	49	5.922	4.489	3.694	3.370	3.206	0.000	0.092	0.075	0.067	0.090	0.375	41.759	0.028	19.236
145453	36	5.740	4.454	4.003	3.898	3.843	0.331	0.067	0.037	0.053	0.148	0.141	43.422	0.143	28.509
145480	40	...	5.235	4.451	4.119	3.722	...	0.143	0.133	0.100	0.154	0.852	76.591	0.397	26.429
150642	2	...	6.463	5.935	5.738	0.036	0.143	0.409	...	0.202	45.019	0.116	10.235
229762	1	...	4.221	3.451	3.093	2.936	...	0.000	0.000	0.000	0.000	0.000	73.744	0.490	23.367
2000 CN105	1	5.498	5.252	0.000	0.000	...	0.000	44.361	0.100	3.422
2002 KY14	2	...	11.362	10.678	9.922	9.651	...	0.043	0.299	0.089	0.127	0.423	12.632	0.318	19.452
2002 PQ152	1	8.886	8.595	0.000	0.000	...	0.000	25.930	0.192	9.334
2002 QX47	12	...	9.341	8.851	8.587	8.096	...	0.176	0.128	0.103	0.000	0.383	25.604	0.375	7.264
2003 QW90	11	...	5.914	5.069	4.588	4.275	...	0.124	0.118	0.096	0.119	0.378	44.024	0.075	10.337
2003 UZ413	6	5.723	4.827	4.259	4.044	4.005	0.000	0.106	0.042	0.037	0.081	0.118	39.401	0.223	12.044
2004 PG115	13	...	5.903	5.080	4.686	4.459	...	0.085	0.151	0.057	0.151	0.568	91.908	0.604	16.277
2004 VT75	1	6.249	5.644	4.961	0.000	0.000	0.000	0.000	39.544	0.213	12.818
2005 CB79	1	...	5.149	4.680	4.558	4.487	...	0.000	0.000	0.000	0.000	0.000	43.167	0.139	28.664
2005 RO43	32	...	7.821	7.193	6.956	6.500	...	0.138	0.097	0.149	0.000	0.429	28.880	0.518	35.415
2005 RS43	47	...	5.691	5.030	4.781	4.448	...	0.129	0.114	0.102	0.179	0.579	48.154	0.203	9.995
2006 QP180	5	...	10.385	9.827	9.215	8.726	...	0.216	0.244	0.229	0.002	0.597	38.600	0.658	4.953
2006 SX368	7	...	10.338	9.694	9.430	9.081	...	0.117	0.054	0.092	0.063	0.146	22.293	0.463	36.283
2007 RT15	4	...	7.213	6.537	6.274	0.153	0.166	0.184	...	0.361	39.662	0.234	12.924
2007 TG422	5	...	7.079	6.305	6.194	0.042	0.193	0.061	...	0.493	549.606	0.935	18.601
2007 TK422	2	...	9.824	9.061	9.128	0.000	0.047	0.000	...	0.067	21.264	0.198	3.066
2007 UM126	2	...	11.121	10.700	10.559	10.067	...	0.141	0.504	0.331	0.000	0.713	12.919	0.340	41.698
2007 VH305	4	...	12.511	12.296	11.961	0.245	0.151	0.226	...	0.328	24.553	0.666	6.205
2008 QB43	1	5.065	4.603	3.874	0.000	0.000	0.000	0.000	43.401	0.220	26.354

NOTE. — Columns description: N_{obs}^r is the number of r -band observations in Table 2; H_u through H_z are the median absolute planetary magnitudes, not corrected for phase angle, in the $ugriz$ bands; u_{StD} through z_{StD} are the StD in H_u through H_z , respectively, but after removing the three bad measurements (see Table 2); and r_{range} is the range in H_r over all measurements, excluding the three bad measurements.

distance Q , the orbital angular momentum in the z -direction ($L_z = \sqrt{a(1-e^2)} \cos I$), and the Tisserand parameter calculated with respect to Neptune ($T_N = \frac{a_N}{a} + 2\sqrt{\frac{a}{a_N}(1-e^2)} \cos I$, where $a_N = 30.104$ AU is the orbital semi-major axis of Neptune).

The only significant correlation reported in the literature is the color-inclination correlation (e.g., Trujillo & Brown; Peixinho et al. 2008). Here, I find only weak evidence for this correlation. Specifically, I find that the $g-r$ colors have a correlation coefficient of -0.90 and -0.68 for scattered disk objects and hot KBOs, respectively. The probability of getting correlation coefficient which are smaller than these values are 1.4% and 2.3% (per trial), respectively. For the rest of the populations investigated here the $g-r$ -inclination correlation one-sided false alarm probability is larger than 2.5% (corresponds to 2σ). The correlation I find is weaker and less significant than that found in other studies. Possible explanations for the differences between the correlations found in this paper and in other works are: (i) the different filters used by

different studies; (ii) selection biases that plague the various samples; and (iii) the small sample size.

The nature of the color-inclination correlation is not clear. Among the possible explanations are collisional resurfacing (Luu & Jewitt 1996; Jewitt & Luu 2001) in which collisions between TNOs expose fresh material and change their colors and at the same time excite their inclinations. Another possibility is that the colors of KBOs are primordial and related to dynamical groupings. However, both explanation have been challenged by observations (see Trujillo & Brown 2002; Volk & Malhotra 2011).

Peixinho et al. (2008) found that there is a break in the “relation” between color and orbital inclination, where objects with $I \lesssim 12$ deg shows no correlation with color. Moreover, the perihelion distance ($= a[1-e]$) and inclination of Classical KBOs are known to be loosely related. I note that the correlation of color with inclination and perihelion distance have a functional resemblance to the functional form of the orbital

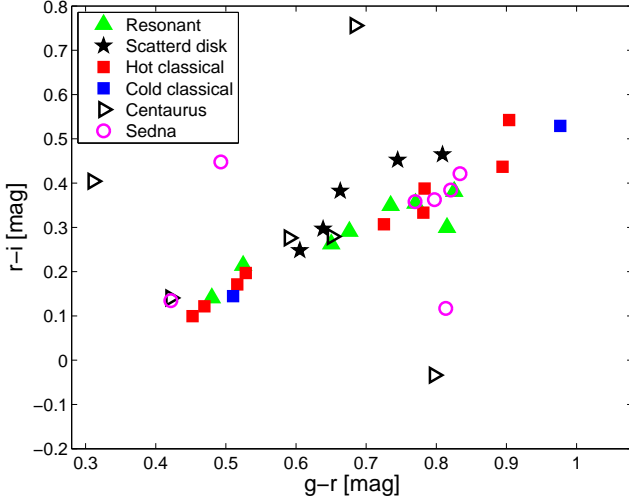


FIG. 2.— The $g-r$ vs. $r-i$ color-color diagram for 37 objects. Different symbols represent distinct classes of objects. Here, I define resonant objects as those having orbital periods within 2.5% of 3/2, 4/3, 2, or 5/2 times the Neptune orbital period. Scattered disk objects are defined as those having $a > 28$ AU, $q < 32$ AU, $Q > 32$ AU and that are not resonant objects. Cold classical objects are defined as those having $a > 30$ AU, $a < 60$ AU, $I < 6$ deg and not being resonant or scattered disk objects. Hot classical are defined similarly to cold classical but having $I > 6$ deg. Centaurus objects are defined as those having $28 \text{ AU} > a > 5.204 \text{ AU}$, and “Sedna”-like objects are all the objects with $a > 60$ AU that are neither resonant objects nor scattered disk objects. I note that some of the various subclasses are not well defined.

angular momentum in the z -direction (L_z)¹⁷. Curiously, I find that the correlation between the $g-r$ color and L_z has a one-sided false alarm probability of 0.4%. It will be interesting to test this correlation using larger samples.

I note that collisions between objects conserve the total angular momentum of the bodies involved in the collision. Since the angular momentum of individual bodies is not conserved, the absolute value of the angular momentum of individual bodies *may* (at least for mostly elastic collisions) statistically increase after a collision. However, this depends on the details of the collisions (e.g., elasticity and initial orbits). Therefore, I cannot rule out that the L_z -color correlation, if real, is a byproduct of TNO collisions. At this stage, it is not clear that the color- L_z correlation really has a physical meaning rather than being a combination of several (physically unrelated) correlations (e.g., color-inclination, and perihelion distance-inclination correlations).

4. VARIABILITY

Thirteen objects in my sample have ten or more SDSS r -band measurements with errors smaller than 0.2 mag. Although the observations are too sparse to unambiguously identify periods, they are good enough to study the objects’ reflectivity as a function of phase angle (§4.1) and to search for large amplitude variability due to rotation and binarity (§4.2).

4.1. Phase angle variations

Solar-System bodies are known to vary in brightness with phase angle. There are two important physical reasons for this variation. The first is shadow hiding, in which particles on the planetary surface cast shadows on adjacent areas: the shaded area is minimized near opposition. The second is an

interference mechanism called coherent backscatter in which reflected light, depending on the regolith properties, may constructively interfere, resulting in an increased brightness at opposition (Hapke 1993; 2002).

Hapke (2002) presented models of these effects. These models have seven degrees of freedom. Given the relatively small number of observations and limited range of phase angles in which the SDSS observations were obtained, I fit a linear relation of the form

$$H_f(\beta) = H_{f,0} + S_f \beta. \quad (1)$$

Here, f is the filter name (g , r or i), $H_{f,0}$ is the absolute planetary magnitude at zero phase angle, S_f is a linearized phase angle slope parameter for filter f , and β is the phase angle. Figure 3 shows $H_r(\beta)$ as a function of β for these 13 objects. As seen in other Solar-System objects, these 13 objects with one exception, are brightest near opposition. To quantify this, in Table 4 I summarize the phase angle slope parameters and related information for the 13 objects. The only object that does not follow this rule is 139775. A plausible explanation is that this object has a large intrinsic variability due to rotation or binarity (see §4.2). I note that the fits are performed only for measurements which $H_r(\beta)$ is within 1 magnitude of the median of $H_r(\beta)$. The three measurements which do not fulfill this condition, and were removed, are indicated in Table 2.

Interestingly, in most cases the slope parameter $H_r(\beta)$ is larger than $0.04 \text{ mag deg}^{-1}$. Such large slope parameters were argued to be the result of coherent backscatter (see Schaefer, Rabinowitz & Tourtellotte 2009).

Although the sample of objects for which I measure the slope parameters is small I attempted to look for correlations between the slope parameters and the orbital parameters of these TNOs. Any hints for correlations found here can be tested in the future using larger samples. The only notable anti-correlations I find are between S_g and a , Q , and P , where P is the orbital period. For example, the correlation between S_g and a is -0.59 , and the probability to get a correlation smaller than this is 1.8% per trial (roughly 2σ significance). In order to test if this correlation is real, larger samples are required. Figure 4 presents S_g as a function of a . This figure suggests that most of the apparent correlation arise due to a difference between objects with large aphelion distances (i.e., “Sedna”-like orbits) and the rest of the population.

This anti-correlation means that the g -band slope parameter is steeper for objects which are closer to the Sun. However, this finding is based on a small sample of only 13 objects. A possible selection bias that may cause such a correlation is that closer objects are visible also on larger phase angles, whereas further objects are visible only near $\beta \approx 0$. Since in reality the derivative of the absolute-magnitude phase-angle relation increases (in absolute value) near opposition, this may introduce the observed anti-correlation between the slope parameter and the semi-major axis. However, most of the SDSS observations were taken near a phase angle of $\beta \cong 1$ deg (see Figure 3). I also note that this selection bias should mostly induce a correlation with q rather than with a or Q , since objects with smaller q are easier to detect. Another possible caveat is that for three objects I find negative g -band slope parameters (see Table 4) presumably affected by measurement errors and/or variability. Therefore, more observations are required in order to confirm the existence of such a correlation.

If this correlation is real, then there are several possible ex-

¹⁷ L_z depends on $\cos(I)$ which varies by only 2% between 0 and 12 deg.

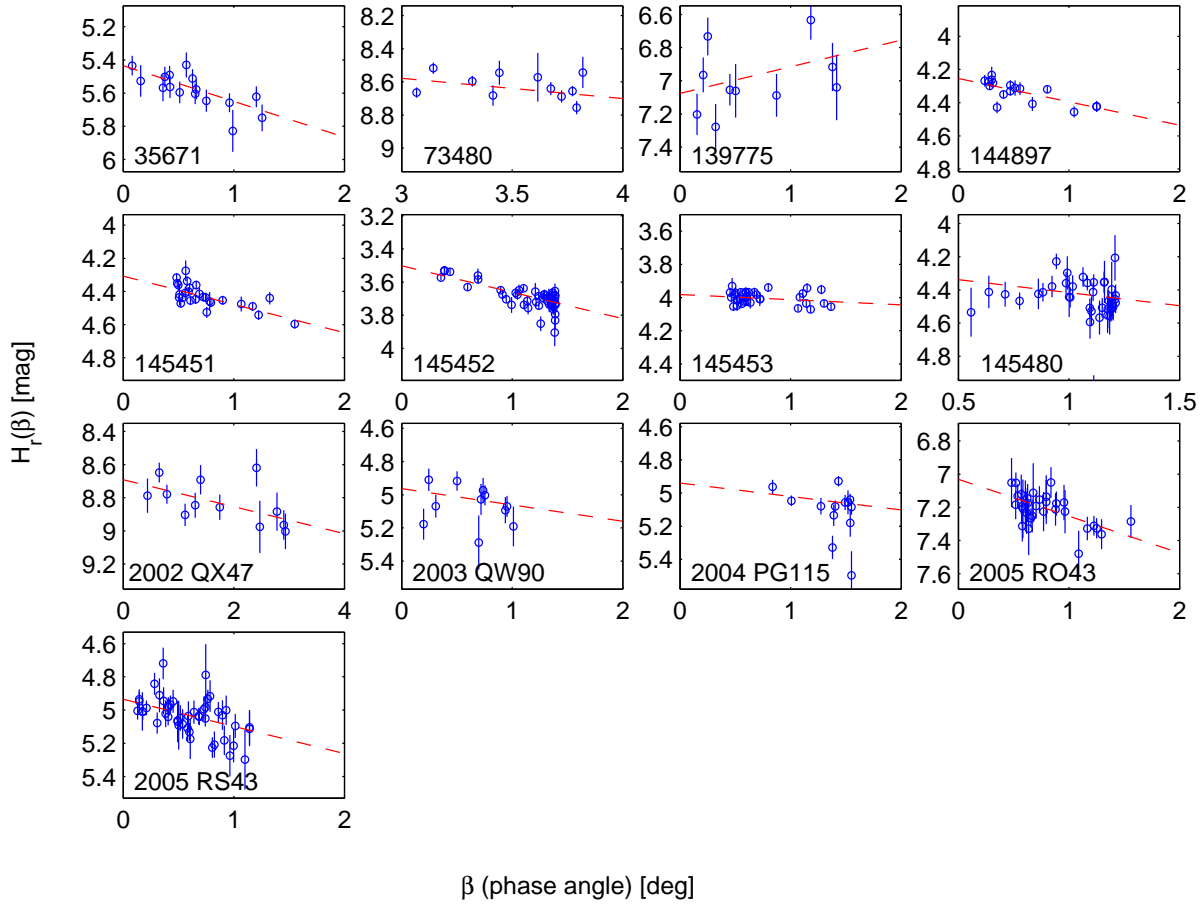


FIG. 3.— Absolute planetary r -band magnitude as a function of phase angle (β). The negative slope parameter of 139775 is presumably due to variability.

TABLE 4
LINEARIZED PHASE ANGLE SLOPE PARAMETERS FOR OBJECTS WITH MULTIPLE OBSERVATIONS

Name	$H_{r,0}$ mag	S_r mag deg $^{-1}$	χ_r^2	dof_r	$H_{g,0}$ mag	S_g mag deg $^{-1}$	χ_g^2	dof_g
35671	5.43 ± 0.04	0.215 ± 0.053	10.6	14	6.02 ± 0.04	0.111 ± 0.058	27.5	14
73480	8.21 ± 0.15	0.122 ± 0.043	21.6	9	8.83 ± 0.16	0.128 ± 0.046	28.4	8
139775	7.08 ± 0.07	-0.161 ± 0.092	20.0	8	7.66 ± 0.30	0.224 ± 0.484	0.0	0
144897	4.25 ± 0.01	0.141 ± 0.023	28.4	15	5.03 ± 0.02	0.195 ± 0.030	29.4	15
145451	4.31 ± 0.02	0.171 ± 0.020	61.9	25	4.78 ± 0.02	0.096 ± 0.022	121.6	25
145452	3.50 ± 0.01	0.160 ± 0.011	91.1	46	4.26 ± 0.02	0.184 ± 0.017	108.2	45
145453	3.98 ± 0.01	0.031 ± 0.015	65.6	33	4.49 ± 0.01	-0.038 ± 0.017	125.1	33
145480	4.26 ± 0.08	0.157 ± 0.078	70.2	37	5.24 ± 0.12	-0.035 ± 0.107	59.8	32
2002 QX47	8.69 ± 0.05	0.081 ± 0.029	15.1	10	9.20 ± 0.06	0.116 ± 0.036	9.1	9
2003 QW90	4.96 ± 0.06	0.098 ± 0.085	14.4	9	5.92 ± 0.09	-0.028 ± 0.142	5.9	6
2004 PG115	4.94 ± 0.07	0.081 ± 0.054	48.4	11	6.05 ± 0.13	-0.112 ± 0.096	7.0	10
2005 RO43	7.03 ± 0.05	0.222 ± 0.056	18.9	30	7.66 ± 0.06	0.155 ± 0.067	40.5	24
2005 RS43	4.94 ± 0.02	0.163 ± 0.038	57.6	45	5.60 ± 0.03	0.126 ± 0.047	76.3	38

NOTE. — Mean photometric properties and slope parameters for the 13 outer Solar-System objects with more than nine SDSS observations. The fits are performed only using measurements with photometric errors smaller than 0.2 mag. Therefore, the g -band and r -band slope measurements are not always based on data points taken at the same epochs. Column descriptions: $H_{f,0}$ is the best fit absolute planetary magnitude at zero phase angle for filter f ; S_f is the linearized slope parameter; χ_f^2 and dof_f indicate the χ^2 and the number of degrees of freedom of the best fit for filter f .

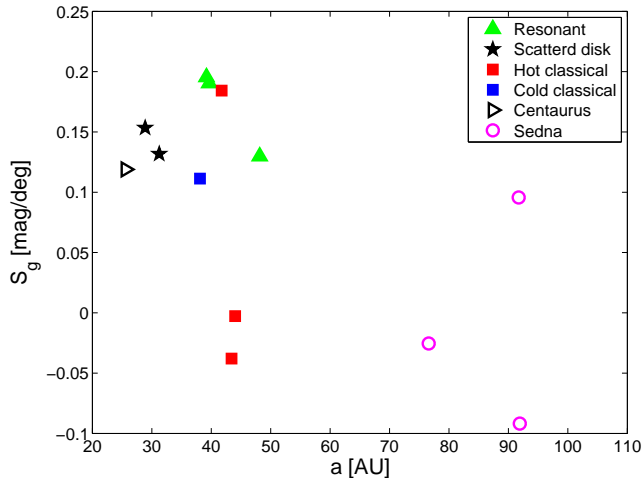


FIG. 4.— The linearized g -band slope parameter S_g as a function of the semi-major axis a of the 13 objects with more than nine photometric measurements. Symbols as in Fig. 2. The typical errors in S_g are roughly $0.05 \text{ mag deg}^{-1}$ (see Table 4).

planations: (i) the regolith or surface composition properties of TNOs vary with distance from the Sun; or (ii) “Sedna”-like objects have distinctive surface properties which are related to their origin. The variation in surface properties as a function of distance from the Sun can originate, for example, if there are variations in the impact rate with micro-meteoroids as a function of heliocentric distance, or due to the crystallization properties of some ices. Based on the Voyager-I and II spacecraft measurements, Gurnett et al. (2005) argued that the number density of dust particles, as a function of heliocentric distance, is roughly uniform (up to distance of about 100 AU). Since the typical orbital speed of objects at 90 AU is 0.6 of that of objects at 30 AU from the Sun, this implies that the micro-meteoroids impact rate does not change dramatically for objects in my sample.

As different ices freeze at different temperatures, the surface properties may also be affected by the equilibrium temperature¹⁸ and escape velocity from the object (e.g., Schaller & Brown 2007). For an albedo of $A = 0.04$, the equilibrium temperature varies between about 50 K at 30 AU from the Sun to 29 K at a heliocentric distance of about 90 AU. However, the three “Sedna”-like objects shown in the right-hand side of Figure 4 are 145451, 145480 and 2004 PG115. During the SDSS observations, these objects were near perihelion at distances of 35, 46 and 36 AU from the Sun, respectively. Therefore, their actual equilibrium temperature, at the time of observations, were similar to those of some of the other objects in Figure 4.

I conclude that differences in surface properties induced by the current orbit of these objects are unlikely. However, I cannot rule out that “Sedna”-like objects have a different origin than some of the other classes of TNOs.

I note that Schaefer et al. (2009) found a significant correlation between the slope parameter (near phase angle of $\beta \cong 1 \text{ deg}$) and the $B - I_c$ color index and also a possible excluded region in the slope parameter vs. inclination phase

space. I do not find any indication for such correlations. However, the Schaefer et al. (2009) sample is larger (35 objects) and contains more diverse planetary objects including the largest KBOs.

4.2. Variability due to rotation and binarity

Table 3 and Figure 3 suggest that some of the objects in the catalog presented here are variable. The variability of these sources may be the result of one or more of the following reasons: Small minor planets, probably with radii smaller than $\sim 100 \text{ km}$, may have irregular shapes and therefore are variable. Moreover, TNOs may show variations due to inhomogeneous surfaces. Alternatively, fast rotation of objects held by their own gravity (i.e., radii larger than $\sim 100 \text{ km}$) may induce a highly non-spherical equilibrium configuration and therefore large amplitude variations (e.g., Leone et al. 1984; Rabinowitz et al. 2006). Finally, contact binaries may show prominent eclipses (e.g., Sheppard & Jewitt 2004; Gnat & Sari 2010).

Objects of 100 km radius with an albedo of 0.04 (0.1) will have absolute planetary magnitude of 7.6 (6.6). Therefore, most of the objects in Table 4 are probably larger than 100 km. In this case, it is probable that large amplitude variations are either due to fast rotation, inhomogeneous surface albedo, or binarity. Since all these possibilities are interesting, photometric follow-up observations of the most highly variable sources in Tables 3 and 4 are desirable.

5. SUMMARY

I cross-correlate SDSS observations with the ephemerides of Solar-System bodies with $a > 10 \text{ AU}$. I present a catalog of SDSS photometric and astrometric measurements of such minor planets based on SDSS observations. After removing possible contaminated measurements. I am left with 388 observations of 42 unique objects.

I find weak evidence for the previously reported inclination-color correlation in the scattered disk objects and hot classical KBOs. I find marginally stronger correlation between the $g - r$ color and orbital angular momentum in the z direction, L_z , of the entire population studied here. I note that a correlation with L_z is consistent with the finding of Peixinho et al. (2008) that objects with inclination below about 12 deg shows no color-inclination correlation.

Finally, the method presented here to collect photometric observations of minor planets in surveys which were not designed for Solar-System observations can be utilized in other ongoing and planned surveys such as the Palomar Transient Factory (Law et al. 2009; Rau et al. 2009), Pan-STARRS (Kaiser et al. 2002), SkyMapper (Keller et al. 2007), and LSST (Tyson et al. 2003).

I thank Orly Gnat, Peter Goldreich, Re’em Sari, and Hilke Schlichting for valuable discussions, and I am greatfull to an anonymous referee for useful suggestions. EOO is supported by an Einstein fellowship and NASA grants.

REFERENCES

¹⁸ The equilibrium temperature of a reflective body in the Solar System is $\cong 278(1 - A)^{1/4}(R/1 \text{ AU})^{-1/2} \text{ K}$, where A is the object’s geometric albedo and R is its distance from the Sun.

Abazajian, K. N., et al. 2009, ApJS, 182, 543
Almeida, A. J. C., Peixinho, N., & Correia, A. C. M. 2009, A&A, 508, 1021

- Bernstein, G. M., Trilling, D. E., Allen, R. L., Brown, M. E., Holman, M., & Malhotra, R. 2004, *AJ*, 128, 1364
- Cooper, J. F., Christian, E. R., Richardson, J. D., & Wang, C. 2003, *Earth Moon and Planets*, 92, 261
- Delsanti, A. C., Boehnhardt, H., Barrera, L., Meech, K. J., Sekiguchi, T., & Hainaut, O. R. 2001, *A&A*, 380, 347
- Dones, L., Weissman, P. R., Levison, H. F., & Duncan, M. J. 2004, *Star Formation in the Interstellar Medium: In Honor of David Hollenbach*, 323, 371
- Duncan, M., Quinn, T., & Tremaine, S. 1987, *AJ*, 94, 1330
- Efron, B., 1982, *The Jackknife, the Bootstrap and Other Resampling Plans*, (The Society for Industrial and Applied Mathematics)
- Efron, B., Tibshirani, R.J., 1993, *An Introduction to the Bootstrap*, Monographs on statistics and applied probability 57, (Chapman & Hall)
- Elliot, J. L., et al. 2005, *AJ*, 129, 1117
- Farinella, P., & Davis, D. R. 1996, *Science*, 273, 938
- Fernández, J. A. 1997, *Icarus*, 129, 106
- Fernández, J. A., & Brunini, A. 2000, *Icarus*, 145, 580
- Fuentes, C. I., & Holman, M. J. 2008, *AJ*, 136, 83
- Gaudi, B. S., & Bloom, J. S. 2005, *ApJ*, 635, 711
- Gnat, O., & Sari, R. 2010, *ApJ*, 719, 1602
- Goldreich, P., Lithwick, Y., & Sari, R. 2002, *Nature*, 420, 643
- Gurnett, D. A., Wang, Z. Z., Persoon, A. M., & Kurth, W. S. 2005, *LPI Contributions*, 1280, 63
- Hainaut, O. R., & Delsanti, A. C. 2002, *A&A*, 389, 641
- Ivezić, Ž., et al. 2001, *AJ*, 122, 2749
- Kaiser, N., et al. 2002, *Proc. SPIE*, 4836, 154
- Keller, S. C., et al. 2007, *PASA*, 24, 1
- Lasker, B. M., et al. 2008, *AJ*, 136, 735
- Law, N. M., et al. 2009, *PASP*, 121, 1395
- Leone, G., Paolicchi, P., Farinella, P., & Zappala, V. 1984, *A&A*, 140, 265
- Luu, J., & Jewitt, D. 1996, *AJ*, 112, 2310
- Morbidelli, A., & Brown, M. E. 2004, *Comets II*, 175
- Moro, D., & Munari, U. 2000, *A&AS*, 147, 361
- Noll, K. S., Stephens, D. C., Grundy, W. M., Osip, D. J., & Griffin, I. 2004, *AJ*, 128, 2547
- Ofek, E. O. 2008, *PASP*, 120, 1128
- Oort, J. H. 1950, *Bull. Astron. Inst. Netherlands*, 11, 91
- Padmanabhan, N., et al. 2008, *ApJ*, 674, 1217
- Pan, M., & Sari, R. 2005, *Icarus*, 173, 342
- Peixinho, N., Lacerda, P., & Jewitt, D. 2008, *AJ*, 136, 1837
- Pier, J. R., Munn, J. A., Hindsley, R. B., Hennessy, G. S., Kent, S. M., Lupton, R. H., & Ivezić, Ž. 2003, *AJ*, 125, 1559
- Porter, S. B., Desch, S. J., & Cook, J. C. 2010, *Icarus*, 208, 492
- Rabinowitz, D. L., Barkume, K., Brown, M. E., et al. 2006, *ApJ*, 639, 1238
- Rau, A., et al. 2009, *PASP*, 121, 1334
- Reid, I. N., et al. 1991, *PASP*, 103, 661
- Romanishin, W., Tegler, S. C., & Consolmagno, G. J. 2010, *AJ*, 140, 29
- Santos-Sanz, P., Ortiz, J. L., Barrera, L., & Boehnhardt, H. 2009, *A&A*, 494, 693
- Schaefer, B. E., Rabinowitz, D. L., & Tourtellotte, S. W. 2009, *AJ*, 137, 129
- Schaller, E. L., & Brown, M. E. 2007, *ApJL*, 659, L61
- Schlichting, H. E., Ofek, E. O., Wenz, M., Sari, R., Gal-Yam, A., Livio, M., Nelan, E., Zucker, S. 2010, *Nature*, in press
- Sheppard, S. S., & Jewitt, D. 2004, *AJ*, 127, 3023
- Sheppard, S. S. 2010, *AJ*, 139, 1394
- Stephens, D. C., et al. 2003, *Earth Moon and Planets*, 92, 251
- Tegler, S. C., & Romanishin, W. 2003, *Icarus*, 161, 181
- Trujillo, C. A., & Brown, M. E. 2002, *ApJL*, 566, L125
- Tucker, D. L., et al. 2006, *Astronomische Nachrichten*, 327, 821
- Tyson, J. A., Wittman, D. M., Hennawi, J. F., & Spergel, D. N. 2003, *Nuclear Physics B Proceedings Supplements*, 124, 21
- Volk, K., & Malhotra, R. 2011, *arXiv:1104.4967*
- Weidenschilling, S. J. 2002, *Icarus*, 160, 212
- York, D. G., et al. 2000, *AJ*, 120, 1579